Peering into water splitting mechanism of g-C₃N₄-carbon dots metal-free photocatalyst

Dan Qu[a], Juan Liu[b], Xiang Miao[d,e], Mumei Han[b], Haochen Zhang[a], Ze Cui[a], Shaorui Sun[a], Zhenhui Kang[b,*], Hongyou Fan[c,*], Zaicheng Sun[a,*]

[a] *Beijing Key Laboratory of Green Catalysis and Separation, Department of Chemistry and Chemical Engineering, School of Environmental and Energy, Beijing University of Technology, 100 Pingleyuan, Chaoyang District, Beijing 100124, PR China*
[b] *Jiangsu Key Laboratory for Carbon-based Functional Materials and Devices, Institute of Functional Nano and Soft Materials (FUNSOM), Soochow University, Suzhou 215123, PR China*
[c] *Sandia National Laboratories, Advanced Materials Laboratory, 1001 University Blvd SE, Albuquerque, NM 87106, USA*
[d] *State Key Laboratory of Luminescence and Applications, Changchun Institute of Optics Fine Mechanics and Physics, Changchun, Jilin 130033, PR China*
[e] *University of Chinese Academy of Sciences, Beijing 100000, PR China*

ARTICLE INFO

ABSTRACT

Photocatalytic water splitting is considered as one of the promising ways to provide clean fuels. Extensive efforts have been made in the past to develop various inorganic and organic materials systems as photocatalysts for water splitting by using visible light. Among these photocatalysts, it was recently demonstrated that incorporation of carbon dots (CDs) into graphitic carbon nitride (g-C₃N₄) results in new metal-free composites (g-C₃N₄-C) with excellent stability and impressive performance for photocatalytic water splitting. However, fundamental questions still remain to be addressed such as how added CDs influence the photocatalytic reaction through the bandgap tunability, charge transfer route and efficiency, as well as the specific function of CDs in the photocatalytic process. Understanding the chemical and physical behaviors of added CDs for the control of g-C₃N₄-C architecture is a critical need for its emergence from fundamental design of more efficient photocatalysts to practical applications. In this article, we report new materials with well-controlled architecture allowing for fine-tuning band gaps for broader visible light absorption and controlled understanding of the photocatalytic process. The well-defined model materials allow us to address the fundamental question regarding chemically bonding of CDs and how the chemical bonded CDs promote charge separation and transfer for highly efficient generation of H₂.

1. Introduction

Photocatalytic water splitting is considered as one of the promising ways to provide clean fuels [1–5]. Extensive efforts have been made in the past to develop various inorganic and organic materials systems as photocatalysts for water splitting by using visible light [2,6–8]. Among these photocatalysts, it was recently demonstrated that incorporation of carbon dots (CDs) into graphitic carbon nitride (g-C₃N₄) resulted in new metal-free composites (g-C₃N₄-C) with excellent stability and impressive performance for photocatalytic water splitting [9]. Through the incorporation of CDs, it was shown that addition of CDs increase the quantum efficiency (QE) and solar-to-hydrogen (STH) efficiency; further, the addition of CDs help to prevent g-C₃N₄ from being poisoned by decomposing of produced H₂O₂. Finally, instead of the conventional four electron step, it makes the photocatalytic reaction proceeds via

stepwise two-electron two steps with reduced system energy in which g-C₃N₄ is essentially responsible for the first step photocatalysis-photocatalytic generation of H₂ while the CDs are responsible for the second step chemical catalysis-decomposition of H₂O₂. However, despite the high performance, the role of CDs associated with chemical and physical processes during the photocatalytic reaction is not yet completely understood. Fundamental questions still remain to be addressed, such as how the added CDs influence the photocatalytic reaction through tuning their band gaps, charge transfer route and efficiency, as well as the specific function of CDs in the photocatalytic process. Understanding the chemical and physical behaviors of the added CDs for ultimate control of g-C₃N₄-C architecture is a critical need for its emergence from fundamental design of more efficient photocatalysts to practical applications.

Extending far beyond the current literature, here we report new

---

materials synthesized by using a homogeneous thermal pyrolysis method in the melted solution, which results in well-controlled architecture allowing for the understanding of the photocatalytic process. In particular, through controlled loading of CDs into g-C_3N_4 then formed g-C_3N_4-C composites, we discover that band gaps of the resulting composites can be finely tuned to extend the solar absorption spectra more broadly to achieve higher QE. Through investigation of charge carriers dynamics, we reveal that the photo-generated electron by g-C_3N_4 under light irradiation rapidly transfer to the CDs with high electron transfer efficiency (96%). Strikingly, we discover that the CDs work not only as a catalyst for H_2O_2 decomposition effectively preventing g-C_3N_4 from H_2O_2 poisoning but also as a co-catalyst for the H_2 generation, which has not been reported before. Because of the controlled architecture of the g-C_3N_4-C composites, we are able to quantify the specific contribution of CDs to the overall H_2 generation and H_2O_2 decomposition, respectively.

2. Results and discussion

2.1. Synthesis of g-C_3N_4-C photocatalysts

g-C_3N_4-C photocatalysts were synthesized through a one-step homogeneous thermal pyrolysis by melting citric acid (CA) and urea powders together under controlled temperature. CA was generally used as the precursor for forming graphitic CDs [10–12] and urea was used as the precursor for the polymerization of g-C_3N_4 network [5,13–15]. CDs with capped urea could form in the melted CA/urea solution at the temperature ranging from 200 to 300 °C. Thus, the loading of CDs in the final g-C_3N_4-C composites can be readily controlled by the added amount of CA. Video S1 records the *in-situ* thermal pyrolysis synthesis process of g-C_3N_4-C_x, (x is the added CA weight percentage of overall urea amount added in the reaction) through melting urea from room temperature to 320 °C. During the reaction, urea was gradually melted upon heating from room temperature to ~110 °C, forming a clear yellow liquid in which CA uniformly dissolved. CA started to form graphitic CDs when the temperature is higher than ~140 °C, and continue to grow to a size of ~7.0 nm as the reaction proceeds [16]. As the temperature continues to rise, CDs in the solution evolve with the condensation polymerization of urea, which is indicated by the release of ammonium gas. According to previous reports [17–19], polymerization of pure urea undergoes from the formation of dimer and melamine followed by the release of ammonium gas and finally polymerized into a g-C_3N_4 network. Because the gradual polymerization process of urea occurred simultaneously with CDs formation in the solution, resulting CDs uniformly distributed in the final g-C_3N_4-C composites.

We performed *in-situ* spectral studies to follow the evolution process of CDs during the thermal pyrolysis. Figs. 1a and S1 show the typical UV–vis spectra of g-C_3N_4-$C_{0.05}$ composites at different temperatures in liquid urea. The spectra exhibit characteristic absorption spectra of chemically bonded N-doped CDs [16]. They have multiple absorption bands centered at $P_1 = \sim 267$ nm, $P_2 = \sim 333$ nm, and $P_3 = \sim 406$ nm. P_1 and P_2 are associated with $\pi \rightarrow \pi^*$ and $n \rightarrow \pi^*$ transitions of C=C and C=O bonds in N-doped CDs, respectively [16]. P_3 represents the typical absorption of a conjugated aromatic C=N system [20]. The decreasing intensity of P_2 band and increasing intensity of P_1 and P_3 unambiguously establishes that CA is being consumed to form CDs that are chemically bonded with g-C_3N_4 as the reaction temperature increases. We found that the CDs grow to a larger size with the increase of reaction time, consistent with previous reports [16,21]. Fig. 1b displays the typical photoluminescent (PL) spectra of g-C_3N_4-$C_{0.05}$ synthesized at 200 °C, excited at different wavelengths. The PL spectra exhibit an emission at ~540 nm that is independent of the excitation wavelengths. The independence of PL suggests that the resultant CDs exhibit uniformly well-defined surface states and single surface functional group [22]. Both UV–vis and PL results strongly indicate that the CDs possess

uniform sp² domain size and surface states [12,23–25]. The uniform surface states of N-doped CDs will essentially simplify the interfacial issue between CDs and g-C_3N_4, for understanding the photocatalytic mechanism of g-C_3N_4-C composites. N_2 isothermal sorption results (Figs. 1c and S2) indicate that g-C_3N_4-C_x composites have a relative high Brunauer-Emmett-Teller (BET) surface areas ($\sim 80 \, m^2 \, g^{-1}$), the surface area of pristine g-C_3N_4 is $\sim 60 \, m^2 \, g^{-1}$.

Representative transmission electron microscopy (TEM) images (Fig. 1d) of CDs revealed an average CDs size of 2.3 ± 0.7 nm with uniform size distribution (Fig. 1d). High-resolution TEM (HR-TEM) image (Fig. S3) confirms the formation of graphite carbon with lattice fringes of 2.14 Å, which attributes to the (100) plane of graphitic carbon [23]. The graphitic framework is further proved by X-ray diffraction pattern (XRD) pattern and Raman spectra (Fig. S4). The XRD spectrum (Fig. S4a) of the g-C_3N_4-$C_{0.05}$ composite (200 °C) shows two prominent peak at ~28° and ~40° that correspond to the (002) and (100) planes of graphite [26,27]. As shown in Fig. S4b, the Raman spectra (λex = 325 nm) of the g-C_3N_4-$C_{0.05}$ composite (200 °C) reveals two prominent peaks at ~1363 and ~1577 cm^{-1}, corresponding to the documented D and G bands, respectively, which is close to that of graphene, indicating that relatively high-quality CDs are produced [12]. Further experiments with controlled addition of CA indicate that the sizes of resulting CDs are tunable by the amount of CA in the reacting system (Fig. S5: a [2.56 ± 0.21 nm]; b [2.99 ± 0.33 nm]; c [3.81 ± 0.35 nm]; and d [4.67 ± 0.62 nm]), consistent with our previous results [16]. When the reaction temperature rise up to 320 °C, the reaction solution turns into white solid, UV–vis spectrum shows (Fig. S1) the adsorption band at $P_3 = \sim 406$ nm turns stronger than the band at 333 nm. The TEM images (Fig. S6) disclose that much more CDs are easily observed. The reaction temperature was finally increased to 600 °C to synthesize g-C_3N_4-C composites. The liquid urea turned into solid and polymerized into g-C_3N_4-C in the high-temperature region. Because of the incorporation of CDs, g-C_3N_4-C_x composites show much darker color than the pure g-C_3N_4, which displays light yellow. The more CA are added the darker g-C_3N_4-C_x display (Fig. S7). Fig. 1e shows the representative TEM image of as-prepared g-C_3N_4-$C_{0.05}$. The composite exhibits a flaky and ultrathin sheet structure. HR-TEM image (Fig. 1f) reveals the embedded CDs with lattice fringe of 2.14 Å [23]. XRD, FTIR, and X-ray photoelectron spectroscopy spectra (XPS) (Figs. S8–S10) confirm the formation of g-C_3N_4-C_x composites by observing of all characteristics of g-C_3N_4 structure embedded with CDs [28].

2.2. Characterizations of the electronic structure of the composite catalysts

The UV–vis spectra of g-C_3N_4-C_x (Fig. 2a) suggest that the band gaps of g-C_3N_4-C_x can be readily tuned by the amount of the added CA. With the incorporation of CDs into the g-C_3N_4, the absorption band gradually red-shifts towards the visible light region. The optical band gaps of these samples were estimated from plots of the square of Kubelka-Munk functions F(R) *versus* photon energy (Figs. 2b, S11 and Table S1) [29]. One of the most notable features is that the band gap energy turns narrower with the size and amount evolution of CDs. The band gap is changed from 2.84 (g-C_3N_4) [17] to 2.08 eV (g-C_3N_4-$C_{1.0}$) with the incorporation of CDs. This change of band gaps in g-C_3N_4-C_x can be attributed to the extended conjugation length due to the incorporation of a π-conjugated sp² domain of CDs chemically bonded to the melon units (Fig. 1a). That is also confirmed by electron paramagnetic resonance (EPR) results from g-C_3N_4-C_x samples. The single Lorentzian line centered at a g value of 2.0034 (Fig. S12) is identified to lone pair electrons in sp²-carbon in the typical g-C_3N_4 [30] and attributed to an unpaired electron on the carbon atoms of the aromatic rings within π-bonded nanosized clusters [31,32]. The EPR intensity greatly enhances as the CA increases, indicate the increased density state of conduction band after the electron donation from CDs. Results from Density Functional Theory (DFT) calculation further confirm that the band gap of g-C_3N_4-C_x composites can be tuned by the effective sp² domain size of CDs (Fig.

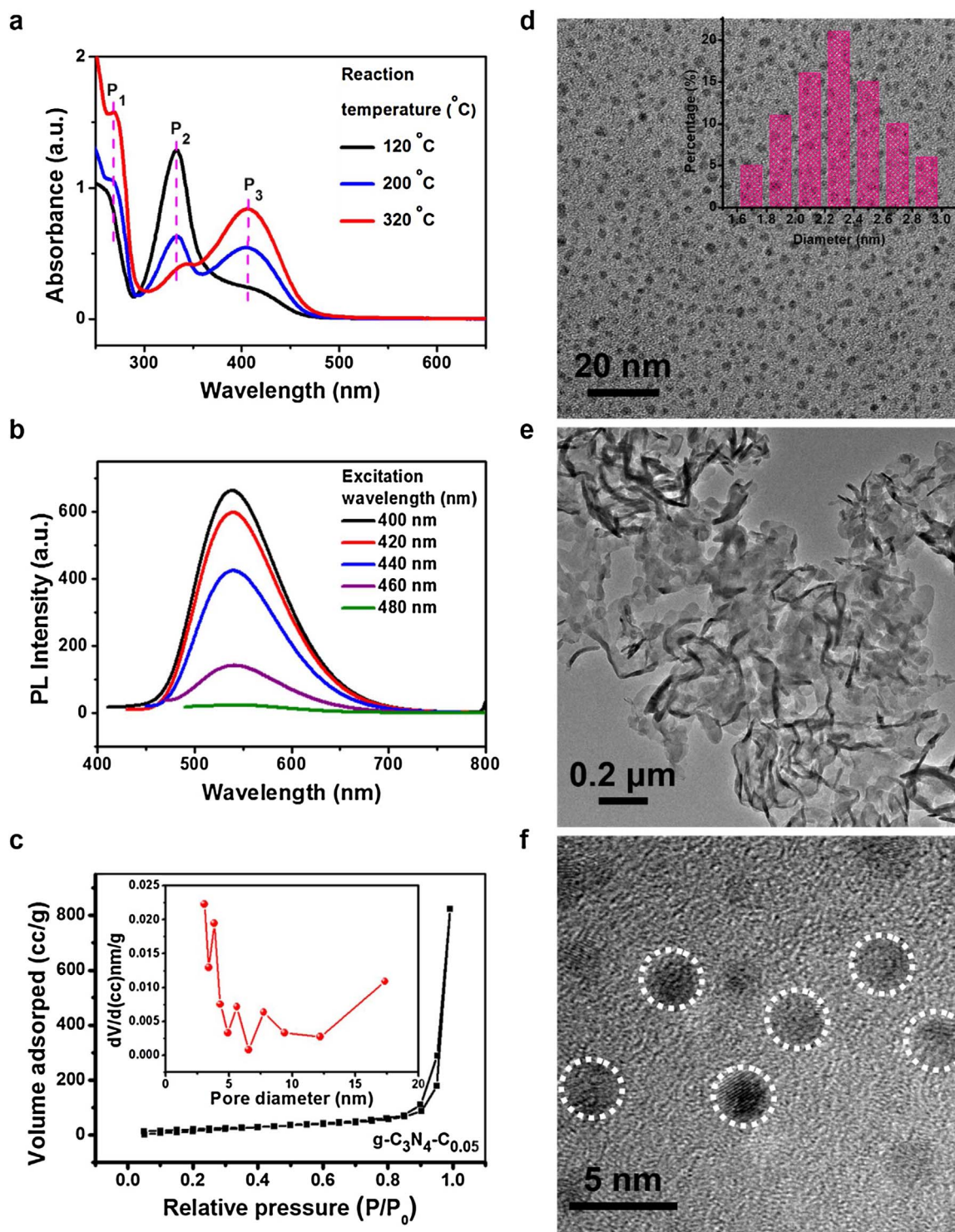**Fig. 1. Structural and optical characterizations of g-C$_3$N$_4$-C$_x$ composites.** (a) UV–vis spectra of g-C$_3$N$_4$-C$_{0.05}$ specimen synthesized at different reaction. (b) PL spectra of g-C$_3$N$_4$-C$_{0.05}$ synthesized at 200 °C at different excitation wavelengths. (c) The specific surface area and pore size distribution of g-C$_3$N$_4$-C$_{0.05}$ (d) Representative TEM image of g-C$_3$N$_4$-C$_{0.05}$ synthesized at 200 °C. Inset is the size distribution of CDs. (e) Representative TEM image and (f) HR-TEM image of g-C$_3$N$_4$-C$_{0.05}$ synthesized at 600 °C.

S13). DFT calculation results clearly show the band gap becomes smaller when CDs were introduced into the g-C$_3$N$_4$. The bigger the size of CDs grows, the narrower the band gap of g-C$_3$N$_4$-C$_x$ becomes. Recently, Wu and coworkers also carried out a similar theoretical calculation [33], and found that the band gaps of g-C$_3$N$_4$-C$_x$ could be engineered by changing the lateral size of CDs and the number of CDs in g-C$_3$N$_4$.

The electronic structure of the g-C$_3$N$_4$-C$_x$ composites was

characterized. The energy levels diagram of the conduction band (CB) and valence band (VB) were determined by the electrochemical method and optical band gap (Fig. S14). The VB maximum was measured by the electrochemical method and the band gap is obtained from the Tauc plot of g-C$_3$N$_4$-C$_x$ (Fig. 2b). The CB was calculated from the VB and band gap values. The CB, VB, and band gap of g-C$_3$N$_4$-C$_{0.05}$ are 0.26, 2.45 and 2.71 eV, respectively. With increasing incorporated CDs, the CB, VB, and band gap of g-C$_3$N$_4$-C$_{1.0}$ change into −0.08, 2.0 and
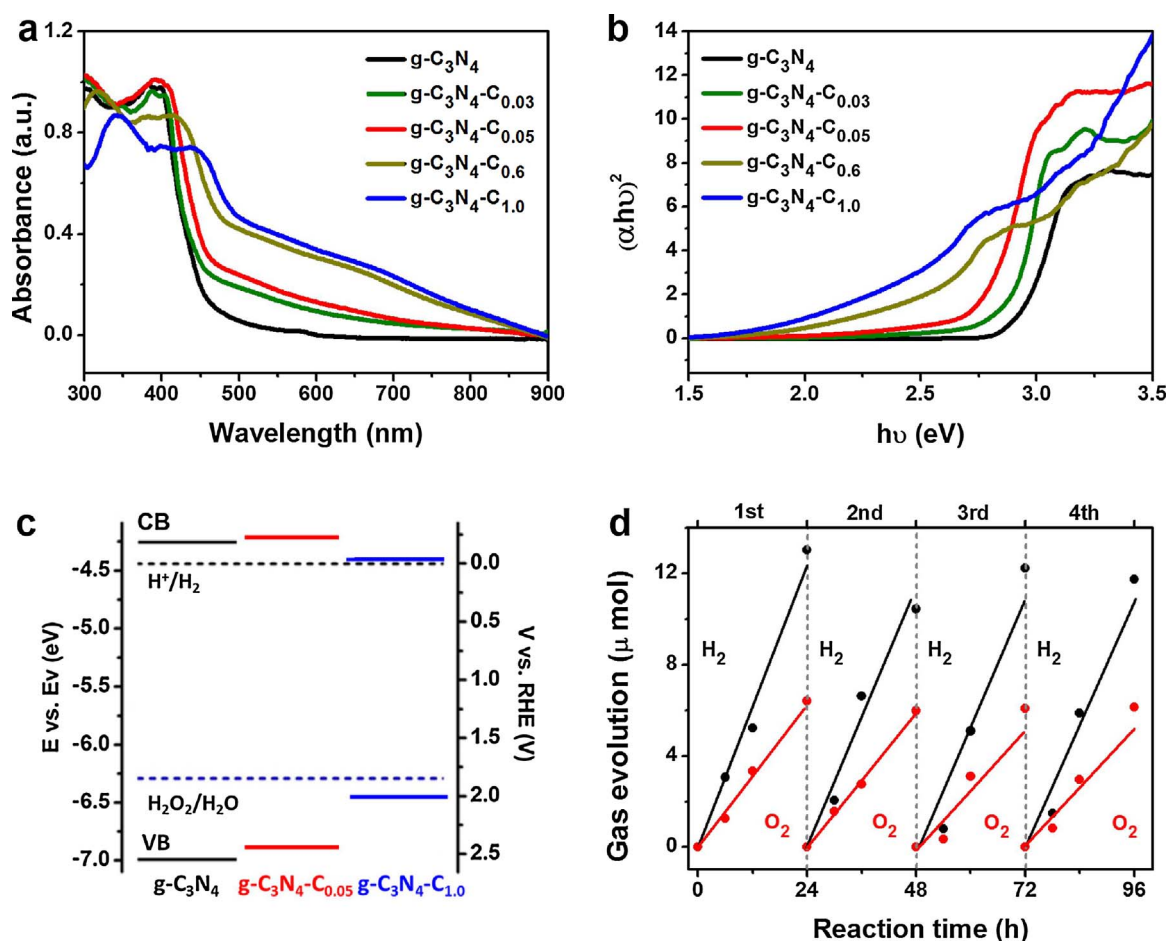
Fig. 2. Characterizations of the electronic structure of the composite catalysts. (a) UV–vis spectra of g-C_3N_4-C_x (x = 0, 0.03, 0.05, 0.6, 1.0) prepared at 600 °C for 3 h. (b) ($\alpha h\upsilon)^2$ *versus hv* curve of g-C_3N_4-C_x (x = 0, 0.03, 0.05, 0.6, 1.0). (c) Band structure diagram for g-C_3N_4-C_x (x = 0, 0.05, 1.0). VB = valence band; CB = conduction band. (d) Typical time course of H_2 and O_2 production from water under visible light irradiation (by a 300-W Xe lamp using a long-pass cutoff filter allowing λ > 420 nm) catalyzed by g-C_3N_4-$C_{0.05}$. (For interpretation of the references to colour in this figure text, the reader is referred to the web version of this article.)

2.08 eV, respectively. Fig. 2c shows that the reduction potential for H_2 is positioned below the conduction band of g-C_3N_4-C_x, and the oxidation level for H_2O–H_2O_2 is above the VB of g-C_3N_4-C_x. These bands are properly positioned allowing for electron and hole – generation and separation for water splitting. Fig. 2d exhibits the photocatalytic performance of g-C_3N_4-$C_{0.05}$ for overall water splitting. It clearly indicates the high performance of overall water splitting from the g-C_3N_4-C composite [9]. The H_2 and O_2 evolution rate is about 5 and 2.5 µmol g^{-1} h^{-1} without any sacrificial agent. Electrochemical measurement (Fig. S15) further confirmed that water-splitting photo-catalysis by g-C_3N_4-C_x proceed *via* two-step 2e$^-$/2e$^-$ process [9]. This suggests that H_2O_2 is produced in the H_2O oxidation step under visible light irradiation and then is catalytically decomposed by CDs.

2.3. Charge separation, transfer route, and efficiency of g-C_3N_4-C photocatalysts

To elucidate the electron and hole separation and transfer route, photo-deposition of metallic Pt and PbO_2 were carried out under visible light irradiation using H_2PtCl_6 and $Pb(NO_3)_2$ precursors, respectively. The HR-TEM image (Fig. 3a) of the photo-deposited g-C_3N_4-$C_{0.05}$ specimen reveal that the reduced metallic Pt nanoparticles with lattice fringe spacing of 2.27 Å are deposited only on CDs with lattice fringe spacing of ~3.0 nm [34]. This specific location of deposited Pt nanoparticles suggests that H_2PtCl_6 precursors get the needed electrons from CDs (not g-C_3N_4) for photo-reduction and formation of Pt nanoparticles. This photo-deposition experiments unambiguously establish that the

photoelectrons generated from g-C_3N_4 under light irradiation transfer to CDs. On the other hand, photo-oxidation of PbO_2 nanoparticles from $Pb(NO_3)_2$ was also performed under visible light irradiation. The HR-TEM image (Fig. 3b) clearly shows PbO_2 nanoparticles with size of ~5.0 nm and lattice fringe spacing of 3.17 Å, which were only deposited on g-C_3N_4 and no CDs was observed near the PbO_2 nanoparticles [34]. Overall, these results suggest that the photo-generated electrons rapidly transfer from g-C_3N_4 to CDs, and holes are mainly kept at the g-C_3N_4 sites.

Photo-generated charges transfer efficiency was also studied during the photocatalytic water splitting. PL spectra of the g-C_3N_4-C_x samples were measured by excitation at λ_{ex} = 395 nm g-C_3N_4 samples exhibit a broad emission peak ~450 nm (Fig. S16). With the incorporation of CDs, the PL intensity of g-C_3N_4-C_x decreases with the increased loading of CA, indicate a suppressed radiation recombination of the photo-induced charge carriers by CDs [35]. This further confirms the role of CDs as an electron acceptor, which is consistent with the observed photoelectron transfer route from g-C_3N_4 to CDs in photo-deposition process of metallic Pt nanoparticles. The PL decays of g-C_3N_4, g-C_3N_4-$C_{1.0}$ and g-C_3N_4 loaded with Pt nanoparticles are shown in Figs. 3c and S17. The average lifetime of g-C_3N_4-C_x rapidly decreases with the increase of CA amount. The PL dynamics of g-C_3N_4 with different loading amounts of CA were investigated. Based on these data and those in Table S2, electron transfer (ET) rate (k_{ET}) and efficiency (η_{ET}) are calculated by using equations in (S1) and (S2). In the case of g-C_3N_4 loaded with 1 wt % Pt nanoparticles, the k_{ET} and η_{ET} are 4.69 × 10^8 s^{-1} and 79.2%, indicating that the electron transfer happens between g-C_3N_4 and Pt
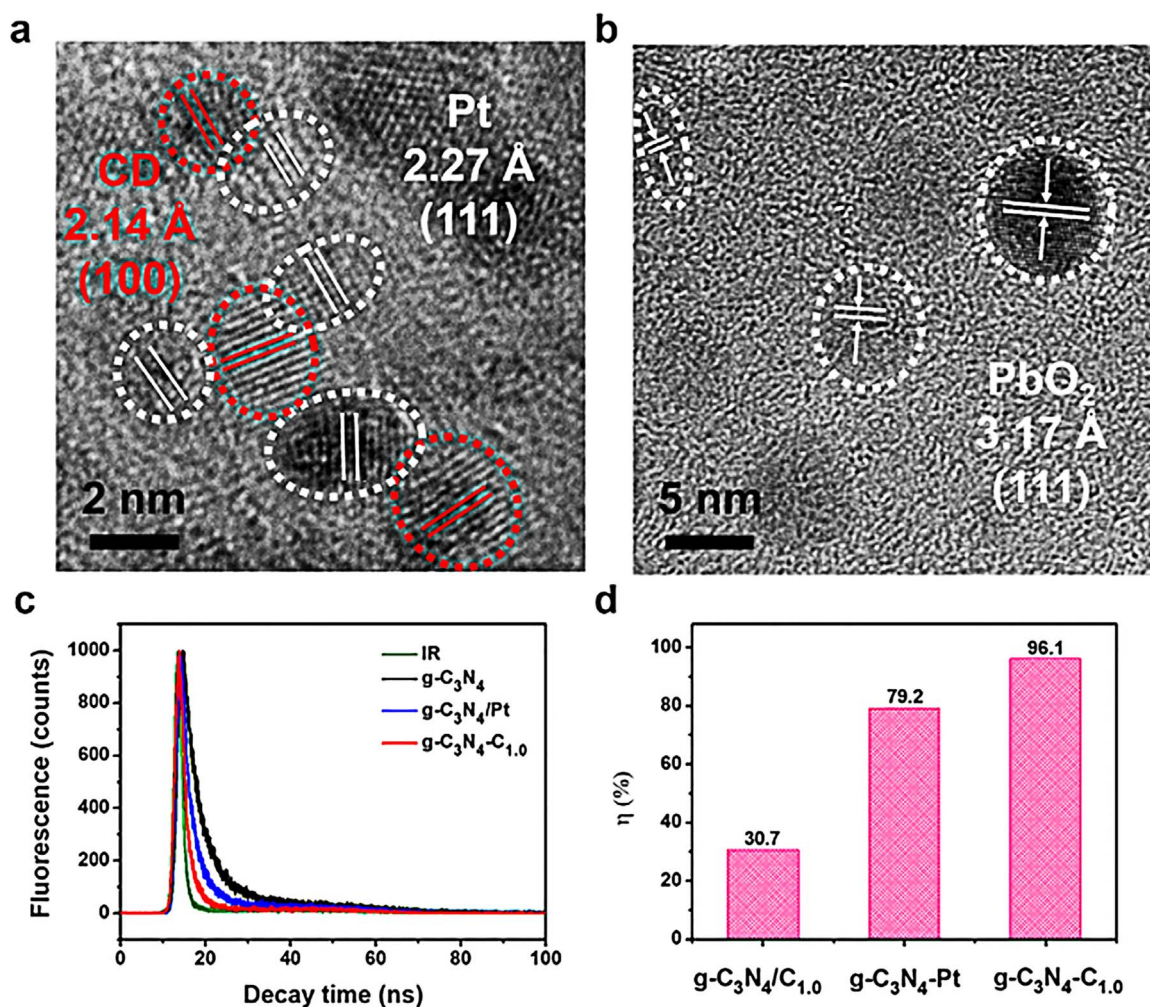
Fig. 3. Charge transfer route and efficiency of g-C₃N₄-C. (a) HR-TEM images of g-C₃N₄-C photo deposited Pt and (b) PbO₂. (c) Photoluminescent lifetime decay of g-C₃N₄-C$_{1.0}$, g-C₃N₄ loaded Pt and g-C₃N₄, respectively. (d) Photo-generated electron transfer rate calculated from the equation (S2).

with a relatively low efficiency. In the case of g-C₃N₄-C$_{0.05}$, both the k_{ET} and η_{ET} reach $4.09 \times 10^8 \, s^{-1}$ and 76.9%, respectively, which are close to the value of g-C₃N₄/Pt. With the increase of the CA, the k_{ET} and η_{ET} of g-C₃N₄-C$_{1.0}$ reach $30.02 \times 10^8 \, s^{-1}$ and 96.1%, respectively. These results indicate the photo-generated electrons transfer from g-C₃N₄ to CDs is much faster and more efficient than that from g-C₃N₄ to Pt. For comparison, g-C₃N₄ physically mixed with CDs were also investigated. The k_{ET} and η_{ET} of g-C₃N₄/C$_{1.0}$ are $0.55 \times 10^8 \, s^{-1}$ and 30.7% for loading ~1.0 wt% CDs onto g-C₃N₄. (Figs. 3d, S17 and Table S2). Above results clearly show the g-C₃N₄-C$_x$ has faster ET rate and higher charge transfer efficiency than those of g-C₃N₄/C$_x$ and g-C₃N₄/Pt due to chemically bonded CDs with g-C₃N₄. The electron transfer from g-C₃N₄ to CDs enables spatial charge separation within g-C₃N₄-C$_x$, with very high overall charge separation efficiency.

2.4. Photocatalytic process with added H₂O₂

Besides an electron acceptor for the H₂ generation, we discover that CDs also possess a role for H₂O₂ decomposition. To understand this, the photo-electrochemical experiment was designed for monitoring the photocurrent changes during the photocatalytic reaction. Fig. 4a shows the photocurrent *v.s.* reaction time plot of g-C₃N₄ and g-C₃N₄-C$_{0.05}$ at different experimental conditions. For pure g-C₃N₄, the dark photocurrent keeps at constant near 0 nA. When the light shines on the g-C₃N₄, the photocurrent is generated with a certain value and gradually decreases and finally reaches near 0 level (Fig. 4a, (1)). This result

suggests that the g-C₃N₄ catalysts possess the photocatalytic activity at the initial stage of the reaction. The decreasing photocurrent is caused by the produced H₂O₂ that poisons the g-C₃N₄, which results in the gradual loss of the photocatalytic activity of g-C₃N₄. For the g-C₃N₄-C$_{0.05}$ case, the photocurrent is generated and maintains at a certain value in a slight fluctuation manner. No photocatalytic activity decay is observed in the case of g-C₃N₄-C$_{0.05}$. It illustrates that g-C₃N₄-C$_{0.05}$ is not poisoned by H₂O₂, which suggests that produced H₂O₂ has been decomposed by the incorporated CDs. We believe the fluctuating photocurrent is the result of balancing between the production and elimination of H₂O₂. When a trace amount of H₂O₂ was deliberately added into the system, a stronger and sharper oscillation was observed at the early stage. As the reaction proceeds, the photocurrent is gradually resumed to the oscillation pattern similar to the case without adding H₂O₂ (Fig. 4a, (2)). This experiment strongly illustrated how the added H₂O₂ influenced the photocurrent. When the added H₂O₂ from the solution reaches the site of the g-C₃N₄-C$_{0.05}$ photocatalyst, it poisons g-C₃N₄ and depresses the photocatalytic activity, reflected by the reducing the photocurrent (Fig. 4a, (3)). As the reaction proceeds, the H₂O₂ is gradually decomposed by the CDs and the photocurrent is resumed. With the continuous consummation of H₂O₂ by photodecomposition, its concentration gradually decreases in the solution, leading to recovering oscillation pattern similar to that without adding H₂O₂ (Fig. 4a, (2)). When H₂O₂ was fully decomposed, the g-C₃N₄-C$_{0.05}$ photocatalysts are recovered to generate photocurrent again (Fig. 4a, (4)).

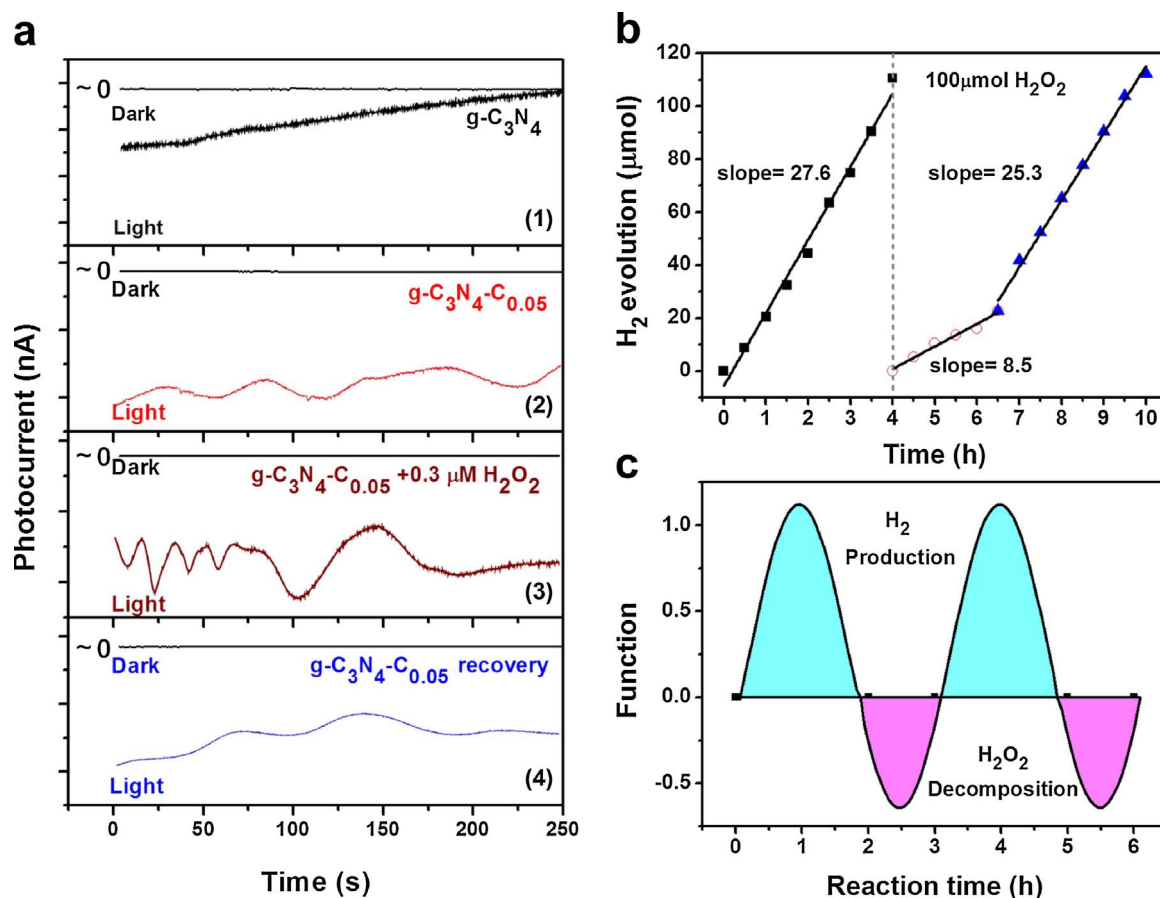To further confirm this, H₂O₂ was added into the H₂ evolution

Fig. 4. Photocatalytic process with added H_2O_2. (a) Photocurrent response of g-C_3N_4 (black), g-C_3N_4-$C_{0.05}$ (red), g-C_3N_4-$C_{0.05}$ with a few drops of 0.3 μmol L^{-1} H_2O_2 (dark red) and after 15 min (blue). (b) Photocatalytic H_2 production of g-C_3N_4-$C_{0.05}$ in a closed system after addition of 100 μmol H_2O_2 into the reaction system at 4 h. (c) The ratio of CDs worked for H_2 production and catalytic H_2O_2 decomposition. It calculated from the (b) and the detailed calculation see part 9 in experimental section in supporting information. (For interpretation of the references to colour in this figure legend, the reader is referred to the web version of this article.)

reaction system in the presence of sacrificial agent Triethanolamine (TEOA) that accepts photo-generated holes to prevent H_2O oxidation and formation of H_2O_2. Fig. 4b shows the time dependence of H_2 evolution before and after H_2O_2 addition. Before adding 100 μmol H_2O_2 into the reaction system, the H_2 evolution rate was ~27.6 μmol h^{-1} (Fig. 4b (1)). The H_2 evolution rate was reduced down to 8.5 μmol h^{-1} when 100 μmol H_2O_2 was added to the reaction system. It took 2.5 h for the H_2 evolution rate going up to 25.3 μmol h^{-1} (Fig. 4b (2)), which indicates that the H_2 evolution rate can fully recover after H_2O_2 completely decomposed. H_2O_2 decomposition rate was calculated to be 57.1 μmol h^{-1} from the above results in Fig. 4b (detailed calculation see supporting information, calculation rate 9). The H_2O_2 decomposition rate is about two times of H_2 evolution rate (27.6 μmol h^{-1}). Given that the H_2O_2 generation rate is same as the H_2 evolution rate because of the same two-electron process, we estimated that it takes two third of the CDs for H_2 production and one third for H_2O_2 decomposition, which is consistent with the H_2 and O_2 evolution rate ratio (Fig. 4c).

Based on all the above results, we conclude that the CDs possess two functions in the photocatalyst, one function is to work as co-catalyst to accept the photo-generated electron from g-C_3N_4 for H_2 generation. Another function is to work as a catalyst for H_2O_2 decomposition. The overall water spitting photocatalytic process contains three continuous steps (i) g-C_3N_4-C photocatalysts adsorb the solar light and generate excited electrons and holes; (ii) the photo-generated electrons are rapidly transferred into the CDs, and then CDs pass the electron to the proton to produce the H_2; (iii) the holes are left on g-C_3N_4 to oxidize water to form H_2O_2 molecule. When H_2O_2 molecule diffuses from the generation site to the CDs site, H_2 production function of CDs will be

depressed because H_2O_2 decomposition rate is faster than H_2 production rate. At this time, the CDs work as a catalyst for decomposing H_2O_2 molecule The H_2 production function will be recovered after the H_2O_2 is decomposed.

3. Conclusions

We have designed a simple one-step homogeneous thermal pyrolysis route to synthesize g-C_3N_4-CDs using CA and urea. Because of the homogeneous liquid reaction environment, the CDs were uniformly embedded in the g-C_3N_4 matrix through chemical bonding. The band gaps of resultant g-C_3N_4-C_x composite photocatalysts have been effectively fine-tuned from 2.84 to 2.08 eV by controlled loading of CA. By tracking the photo-generated electrons and holes transfer route, we showed the photo-generated electron is transferred into the CDs and the corresponding hole remains on the g-C_3N_4. PL and lifetime investigation illustrates that g-C_3N_4-CDs exhibit high charge transfer rate and efficiency due to chemical bonding between g-C_3N_4 and CDs. We demonstrated that CDs have two functions in the g-C_3N_4-C_x composites. One function is the electron acceptor and co-catalyst for H_2 production, the other function is the catalyst for the decomposing H_2O_2 produced by water oxidation. We estimated that one-third of the CDs work as a catalyst for H_2O_2 decomposition and two third as H_2 production. Our findings provide detailed fundamental understandings of chemical and physical processes during photocatalytic water splitting reaction by using g-C_3N_4-C_x composites, which will help to design more robust and high efficient metal-free photocatalysts.

Acknowledgments

Appendix A. Supplementary data

Supplementary data associated with this article can be found, in the online version, at https://doi.org/10.1016/j.apcatb.2018.01.030.

Detailed experimental, more photocatalytic activity measurement, VB UPS, FT-IR and Raman spectra (PDF).

References

[1] X. Chen, A. Selloni, Chem. Rev. 114 (2014) 9281–9282.
[2] K.S. Joya, Y.F. Joya, K. Ocakoglu, R. van de Krol, Angew. Chem. Int. Ed. 52 (2013) 10426–10437.
[3] K. Zhang, L. Guo, Catal. Sci. Technol. 3 (2013) 1672–1690.
[4] M.G. Walter, E.L. Warren, J.R. McKone, S.W. Boettcher, Q. Mi, E.A. Santori, N.S. Lewis, Chem. Rev. 110 (2010) 6446–6473.
[5] W.-J. Ong, L.-L. Tan, Y.H. Ng, S.-T. Yong, S.-P. Chai, Chem. Rev. 116 (2016) 7159–7329.
[6] S.J.A. Moniz, S.A. Shevlin, D.J. Martin, Z.-X. Guo, J. Tang, Energy Environ. Sci. 8 (2015) 731–759.
[7] T. Hisatomi, J. Kubota, K. Domen, Chem. Soc. Rev. 43 (2014) 7520–7535.
[8] H. Wang, L. Zhang, Z. Chen, J. Hu, S. Li, Z. Wang, J. Liu, X. Wang, Chem. Soc. Rev. 43 (2014) 5234–5244.
[9] J. Liu, Y. Liu, N. Liu, Y. Han, X. Zhang, H. Huang, Y. Lifshitz, S.-T. Lee, J. Zhong, Z. Kang, Science 347 (2015) 970–974.
[10] S.N. Baker, G.A. Baker, Angew. Chem. Int. Ed. 49 (2010) 6726–6744.
[11] S. Zhu, Q. Meng, L. Wang, J. Zhang, Y. Song, H. Jin, K. Zhang, H. Sun, H. Wang, B. Yang, Angew. Chem. Int. Ed. 52 (2013) 3953–3957.
[12] D. Qu, M. Zheng, P. Du, Y. Zhou, L. Zhang, D. Li, H. Tan, Z. Zhao, Z. Xie, Z. Sun, Nanoscale 5 (2013) 12272–12277.
[13] J. Liu, T. Zhang, Z. Wang, G. Dawson, J. Mater. Chem. 21 (2011) 14398–14401.
[14] J. Xu, Y. Li, S. Peng, G. Lu, S. Li, Phys. Chem. Chem. Phys. 15 (2013) 7657–7665.
[15] F. Dong, Z. Zhao, T. Xiong, Z. Ni, W. Zhang, Y. Sun, W.-K. Ho, ACS Appl. Mater. Interfaces 5 (2013) 11392–11401.
[16] D. Qu, M. Zheng, L. Zhang, H. Zhao, Z. Xie, X. Jing, R.E. Haddad, H. Fan, Z. Sun, Sci. Rep. 4 (2014) 5294.
[17] Y. Zhang, J. Liu, G. Wu, W. Chen, Nanoscale 4 (2012) 5300–5303.
[18] B.V. Lotsch, W. Schnick, Chem. Mater. 17 (2005) 3976–3982.
[19] B.V. Lotsch, W. Schnick, Chem. Mater. 18 (2006) 1891–1900.
[20] D.J. Martin, K. Qiu, S.A. Shevlin, A.D. Handoko, X. Chen, Z. Guo, J. Tang, Angew. Chem. Int. Ed. 53 (2014) 9240–9245.
[21] S. Qu, X. Wang, Q. Lu, X. Liu, L. Wang, Angew. Chem. Int. Ed. 51 (2012) 12215–12218.
[22] D. Qu, X. Miao, X. Wang, C. Nie, Y. Li, L. Luo, Z. Sun, J. Mater. Chem. B 5 (2017) 4988–4992.
[23] Y. Dong, H. Pang, H.B. Yang, C. Guo, J. Shao, Y. Chi, C.M. Li, T. Yu, Angew. Chem. Int. Ed. 52 (2013) 7800–7804.
[24] Y. Dong, J. Shao, C. Chen, H. Li, R. Wang, Y. Chi, X. Lin, G. Chen, Carbon 50 (2012) 4738–4743.
[25] D. Qu, M. Zheng, J. Li, Z. Xie, Z. Sun, Light-Sci. Appl. 4 (2015) e364.
[26] D. Qu, Z. Sun, M. Zheng, J. Li, Y. Zhang, G. Zhang, H. Zhao, X. Liu, Z. Xie, Adv. Opt. Mater. 3 (2015) 360–367.
[27] M. Zheng, S. Liu, J. Li, D. Qu, H. Zhao, X. Guan, X. Hu, Z. Xie, X. Jing, Z. Sun, Adv. Mater. 26 (2014) 3554–3560.
[28] X. Wang, K. Maeda, A. Thomas, K. Takanabe, G. Xin, J.M. Carlsson,, K. Domen, M. Antonietti, Nat. Mater. 8 (2009) 76–80.
[29] Y.I. Kim, S.J. Atherton, E.S. Brigham, T.E. Mallouk, J. Phys. Chem. 97 (1993) 11802–11810.
[30] J. Zhang, X. Chen , K. Takanabe, K. Maeda, K. Domen, J.D. Epping, X. Fu, M. Antonietti, X. Wang, Angew. Chem. Int. Ed. 49 (2010) 441–444.
[31] J. Zhang, G. Zhang, X. Chen, S. Lin, L. Möhlmann, G. Dołęga, G. Lipner, M. Antonietti, S. Blechert, X. Wang, Angew. Chem. Int. Ed. 51 (2012) 3183–3187.
[32] M. Tabbal, T. Christidis, S. Isber, P. Mérel, M.A.E. Khakani, M. Chaker, A. Amassian, L. Martinu, J. Appl. Phys. 98 (2005) 044310.
[33] Z. Ma, R. Sa, Q. Li, K. Wu, Phys. Chem. Chem. Phys. 18 (2016) 1050–1058.
[34] B. Wang, S. Shen, L. Guo, Appl. Catal. B 166–167 (2015) 320–326.
[35] Y. Ling, G. Wang, J. Reddy, C. Wang, J.Z. Zhang, Y. Li, Angew. Chem. 124 (2012) 4150–4155.